

# Query-Calibrated Segmental Admission for Descriptor-Agnostic LiDAR Loop Closure in Repetitive Environments

Jaehyun Kim, Seungwon Choi, Wonseok Kang, and Tae-Wan Kim

**Abstract**—Structurally repetitive environments produce visually plausible but aliased LiDAR loop candidates that can destabilize pose-graph optimization when admitted as loop factors. We propose Query-Calibrated Segmental Admission (QCSA), a descriptor-agnostic sparse loop-admission policy for graph-stability-oriented insertion. The policy scores short descriptor segments against hard negatives, calibrates which query-level segment hypotheses reach geometry, and inserts representative pairs validated by Generalized Iterative Closest Point (G-ICP). We evaluate it on the SNU Library Dataset (SNULib) and HeLiPR overlap routes. Aggregated over seven LiDAR descriptor families on SNULib, QCSA reduces inserted loop factors by 3.8 $\times$ , raises factor precision from 0.542 to 0.717, and sharply lowers false admissions per query group. With this sparser graph, it maintains comparable mean absolute trajectory error (ATE) and substantially reduces worst-sequence ATE versus dense Top1+G-ICP (1.064 to 0.778 m). The aggregate mean and worst-sequence ATE remain lower than the odometry-only reference. Under a matched factor budget, QCSA also attains lower trajectory error than SeqSLAM and sparse Top1+G-ICP selections. Fixed-transfer validation on HeLiPR, with no route-specific tuning, likewise suppresses hard-negative admissions. These results support the proposed admission layer for aliasing-heavy simultaneous localization and mapping (SLAM). Our implementation and dataset will be released at: [https://github.com/wanderingcar/snu\\_library\\_dataset](https://github.com/wanderingcar/snu_library_dataset).

## I. INTRODUCTION

Autonomous mobile robots (AMRs) are now deployed in factories, warehouses, and service environments to automate repetitive tasks and assist humans. Many commercial AMRs rely on LiDAR as a primary sensor for perception, localization, and mapping. In these systems, a consistent three-dimensional map of the environment is essential.

The quality of this LiDAR-based map depends strongly on accurate loop closure along the robot’s trajectory [1], [2]. LiDAR loop closure typically selects candidates by comparing the similarity of global descriptors between temporally separated point clouds. Numerous LiDAR global descriptors have been proposed in recent years [3]–[6], alongside related place-recognition methods based on local geometric primitives or density-map representations [7], [8]; these methods are commonly evaluated on public LiDAR benchmarks such as [9]–[11]. As a result, global descriptors are now widely used for LiDAR-based place recognition and loop closure in modern simultaneous localization and mapping (SLAM) systems. However, structurally repetitive environments (e.g., warehouse racks, library stacks, industrial corridors) induce



Fig. 1: The book repository at Seoul National University Library, showing repetitive shelving structures. The mobile robot, equipped with a 360-degree LiDAR, stereo camera, and IMU, was used to collect the dataset.

severe perceptual aliasing, as illustrated in Fig. 1 and Fig. 2. In such environments, visually plausible but incorrect candidates can enter pose-graph optimization (PGO) and distort the resulting map [12]–[14]. Robustly disambiguating structurally identical locations therefore remains an open challenge for loop-factor admission.

We propose Query-Calibrated Segmental Admission (QCSA), a descriptor-agnostic sparse loop-admission policy that evaluates hard-negative segment evidence, calibrates query-level hypotheses before geometry, and inserts representative pairs validated by Generalized Iterative Closest Point (G-ICP). We evaluate loop closure as graph-stability-oriented admission: factor precision, false admissions per 1000 query groups, hard-negative admission, G-ICP verification load, sparse-budget PGO behavior, and external transfer to a public overlap benchmark.

In summary, the contributions of our work are threefold:

- A descriptor-agnostic sparse loop-admission layer that combines hard-negative segment evidence, query-level calibration, and representative-pair insertion.
- A graph-level admission evaluation protocol for aliasing-heavy environments, emphasizing false admissions, hard-negative admission, G-ICP load, and same-budget PGO behavior.
- Experiments on SNULib and HeLiPR [15] across seven LiDAR descriptor families, showing that QCSA yields

The authors are with the Department of Naval Architecture and Ocean Engineering, Seoul National University, Seoul, South Korea (e-mail: jaedalong@snu.ac.kr; csw3575@snu.ac.kr; eoid361@snu.ac.kr; tae-wan@snu.ac.kr).

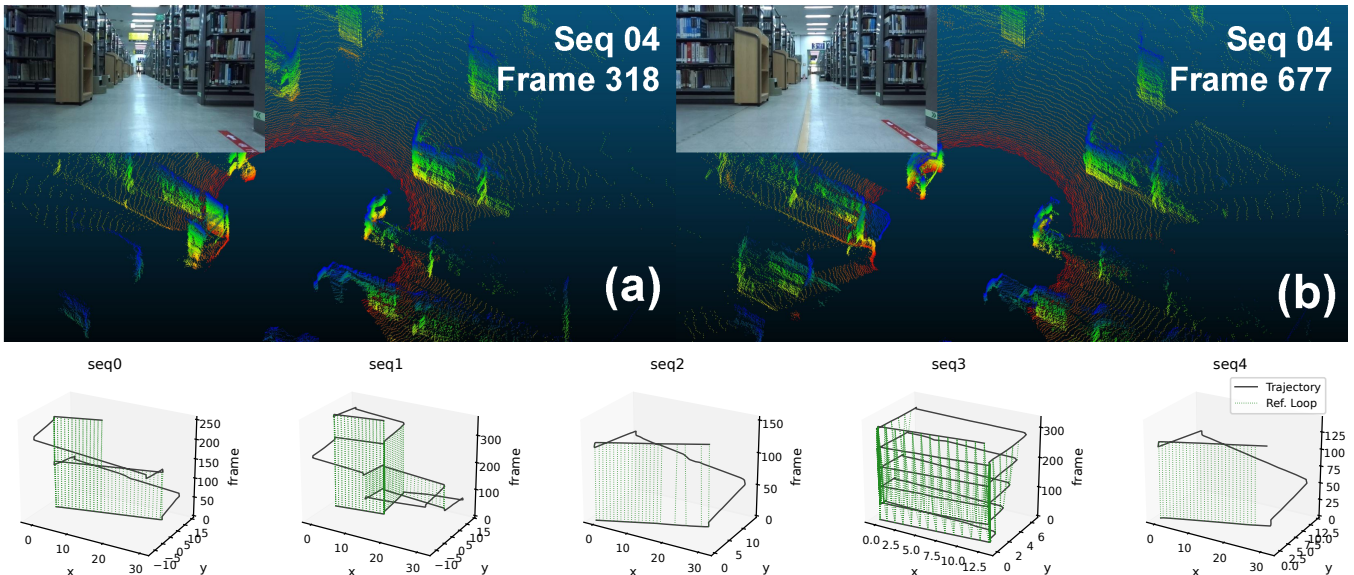


Fig. 2: SNULib samples and trajectory structure. Top: LiDAR scans and camera images for frame 318 (a) and frame 677 (b) in Sequence 04. Although the viewpoints differ by more than 15 m, repeated structures induce nearly identical visual and geometric patterns. Bottom: reference trajectories and reference loop segments for all five library sequences.

a sparser graph with higher loop-factor precision, lower false-admission and G-ICP verification load, improved worst-sequence absolute trajectory error (ATE), and fixed-transfer hard-negative suppression.

## II. RELATED WORK

LiDAR place recognition and loop closure are commonly built on compact global descriptors and related place-recognition pipelines for efficient candidate retrieval. Projection, voxel, handcrafted, segment-based, local-primitive, and learned representations have all been used to summarize single scans or aggregated local maps into scalar or vector evidence for fast candidate search [3], [4], [6], [16]–[23]. These methods primarily improve the retrieval front-end. The proposed layer is complementary: it accepts any scalar descriptor score and acts after retrieval as a graph-admission layer.

Aliasing can also be addressed by adding richer cues, temporal consistency, or statistical evidence aggregation. OverlapNet, OverlapTransformer, and SeqOT improve scan matching with overlap prediction, attention, or sequence information [24]–[26], while SeqSLAM and FAB-MAP show the value of temporal coherence and probabilistic aliasing models in appearance-based place recognition [27], [28]. Our approach follows this practical sequence-consistency view, but uses it as a sparse graph-admission layer: descriptor evidence is aggregated over short local segments and the deployed decision is calibrated at the query level.

Robust loop closure is often handled at the graph level after candidate insertion. Switchable constraints, dynamic covariance scaling, max-mixtures, and related robust pose-graph methods reduce the influence of bad loop factors during optimization [14], [29]–[31]. These methods are important back-end defenses, but they still require loop candidates

to enter the optimization problem and do not reduce front-end G-ICP verification load. The proposed layer acts earlier in the pipeline: it reduces the high-risk aliased candidate stream before geometry, keeps graph insertion sparse, and uses G-ICP as a shared geometric verification step.

## III. METHOD

### A. Overview

The method is a descriptor-agnostic layer for sparse loop-factor insertion. It calibrates which query-level segment hypotheses are allowed to reach geometry while bounding the number of loop factors inserted from each accepted segment.

Let  $k \in \{0, \dots, N-1\}$  index LiDAR keyframes, and let a descriptor extractor  $g(\cdot)$  map the scan  $\mathcal{X}_k$  to a descriptor vector

$$\mathbf{d}_k = g(\mathcal{X}_k). \quad (1)$$

The method operates on a scalar retrieval score  $x(q, t)$ ; when needed, native similarity scores are monotonically transformed so that lower values denote stronger descriptor agreement. This score-level interface allows the verifier to be attached to handcrafted descriptors, learned global descriptors, or sequence descriptors without modifying the descriptor front-end.

For each query  $q$ , a fixed retrieval front-end returns the top- $M$  database candidates  $\mathcal{T}(q)$ . It then applies the following pipeline:

$$\begin{aligned} \text{top-}M \text{ retrieval} &\rightarrow \text{segment score} \rightarrow \text{calibrated boundary} \\ &\rightarrow \text{G-ICP gate} \rightarrow \text{loop factor insertion.} \end{aligned}$$

A central design choice is that the descriptor-evidence stage is calibrated at the query level. When a query has several visually plausible hard negatives, admission is tied to the

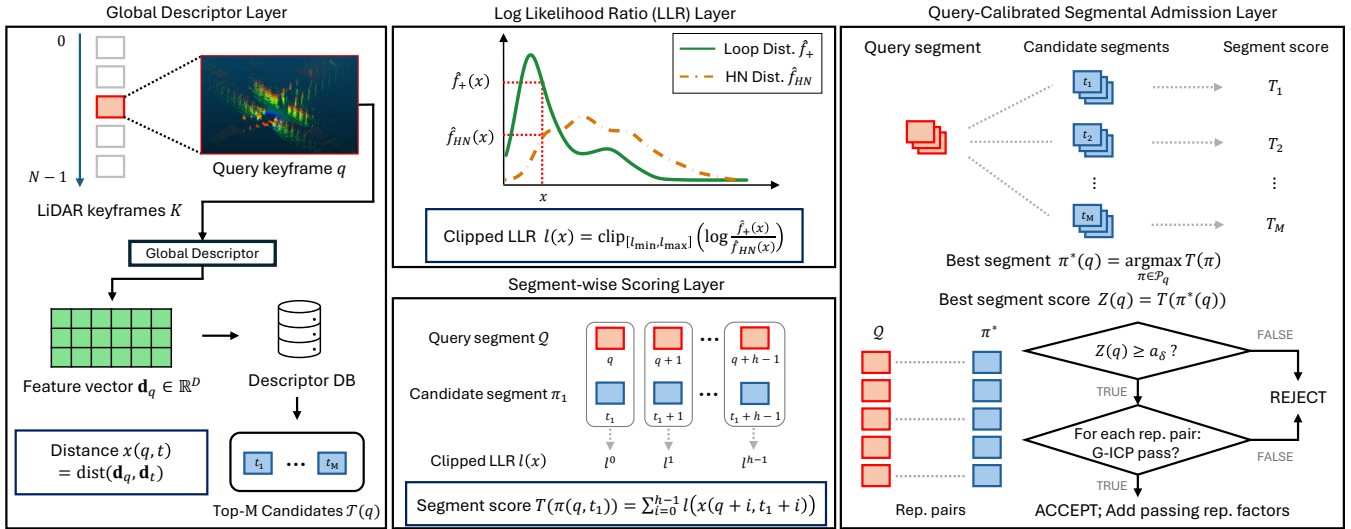


Fig. 3: Proposed loop-admission pipeline. Left: global-descriptor retrieval forms a candidate set for a query keyframe. Middle-right: descriptor distances are mapped to hard-negative log-likelihood evidence, accumulated along short fixed unit-stride segment candidates, filtered by a query-calibrated boundary, and passed to geometric verification before sparse loop-factor insertion. A single forward path is drawn for readability; deployment evaluates the allowed horizons and directions, and inserts only G-ICP-passing representative pairs from the selected segment.

maximum segment evidence before calibration. This couples candidate selection to the query-level admission event rather than to independent pairwise decisions.

### B. Hard-Negative Descriptor Evidence

For each descriptor family, QCSA converts the scalar retrieval score into loop evidence using two score distributions: one from reference loop pairs and one from hard negatives. A hard negative is a non-loop candidate that the same descriptor ranks near the top, which is the typical failure mode in repetitive corridors and shelves. Comparing against this hard-negative distribution keeps the descriptor front-end unchanged while focusing admission on confusable wrong places.

Given a descriptor score  $x$ , we compute a clipped log-likelihood ratio (LLR)

$$\ell(x) = \text{clip}_{[\ell_{\min}, \ell_{\max}]} \left( \log \frac{\hat{f}_+(x)}{\hat{f}_{\text{HN}}(x)} \right), \quad (2)$$

where  $\hat{f}_+$  is the score distribution of reference loop pairs and  $\hat{f}_{\text{HN}}$  is the score distribution of hard negatives; Section IV-B defines the calibration samples and fitting details. The clipping prevents an outlier score from dominating an entire segment. Positive  $\ell(x)$  values support the loop hypothesis, while negative values support the hard-negative hypothesis.

### C. Segment Candidate Construction

Let  $q$  denote the anchor query keyframe index, and let the fixed descriptor front-end return  $\mathcal{T}(q) = \{t_1, \dots, t_M\}$ . For a segment horizon  $h$ , the query-side segment anchored at  $q$  is

$$\mathcal{Q}(q, h) = \{q + i\}_{i=0}^{h-1}. \quad (3)$$

For each retrieved database candidate  $t_m$ , the verifier pairs this query-side segment with a short fixed unit-stride database segment. The resulting candidate path is a sequence of paired keyframe indices

$$\pi(q, t_m; s, h) = \{(q + i, t_m + si)\}_{i=0}^{h-1}, \quad (4)$$

where  $h \in [n_{\min}, n_{\max}]$  is the segment horizon and  $s$  is a fixed unit-stride direction. The main SNULib setting uses  $s \in \{+1, -1\}$ , corresponding to forward and reverse database traversal; the forward-only variant uses  $s = +1$ . The verifier does not perform velocity, offset, or dynamic-time-warping search; it relies on motion-selected SLAM keyframes and the retrieved anchor pair so that adjacent indices approximate local spatial progress. The use of subsequent query keyframes in each query-side segment  $\mathcal{Q}(q, h)$  gives the decision for anchor query  $q$  at most  $n_{\max} - 1$  keyframes of latency. In the SNULib evaluation, each database index in a candidate path must remain at least 25 frames older than its paired query index, so this query-side look-ahead only adds bounded decision latency.

The descriptor evidence for a path is the segment score

$$T(\pi) = \sum_{(q,t) \in \pi} \ell(x(q, t)). \quad (5)$$

The resulting  $T(\pi)$  summarizes descriptor evidence over the candidate sequence. Let  $\mathcal{P}(q)$  denote the set of all segment paths generated from the retrieved candidates, fixed directions, and horizons. For each query, the verifier selects the maximum-score segment:

$$\pi^*(q) = \arg \max_{\pi \in \mathcal{P}(q)} T(\pi), \quad T^*(q) = T(\pi^*(q)). \quad (6)$$

This score is calibrated from hard-negative query maxima on the calibration sequences using the rule in Section III-D, rather than thresholded by a descriptor-specific global constant. The calibration statistic uses the same retrieved candidates, fixed directions, and horizons used at deployment.

#### D. Query-Level Hard-Negative Calibration

The calibration step targets the event that a hard-negative query would pass the descriptor-evidence stage. For each query  $q$ , let

$$Z_q = T^*(q) \quad (7)$$

be the strongest segment score proposed for that query. Given a target hard-negative trigger level  $\delta$ , we set the boundary from ranked calibration scores rather than assuming an analytic score model. For calibration candidate segments with no reference-positive hits, QCSA records the largest segment score  $Z_q$  produced by the descriptor-evidence stage; ambiguous partial-overlap segments are excluded using the label construction in Section IV-B. The boundary is chosen from the upper tail of these maxima so that a controlled fraction  $\delta$  of calibration hard-negative query maxima would trigger the descriptor-evidence stage. We use the finite-sample quantile rule [32]:

$$r = \lceil (n_{\text{cal}} + 1)(1 - \delta) \rceil, \quad a_\delta = Z_{(r)}, \quad (8)$$

where  $n_{\text{cal}}$  is the number of calibration queries and  $Z_{(r)}$  is the  $r$ -th value after sorting the hard-negative query maxima in increasing order; for the operating points used here,  $1 \leq r \leq n_{\text{cal}}$ . At test time, the descriptor-evidence stage triggers when

$$Z_q \geq a_\delta. \quad (9)$$

Under comparable calibration and test hard-negative distributions, this boundary defines an interpretable operating point for query-level segment triggering. This controls the pre-geometry trigger rate; representative-pair selection and the shared G-ICP gate further govern factor insertion.

#### E. Sparse Loop Factor Insertion

For each test query, the verifier first chooses the strongest segment  $\pi^*(q)$  under the fixed descriptor family. If  $Z_q$  is below  $a_\delta$ , the query abstains and no G-ICP verification is run. Otherwise, it admits this calibrated segment and selects representative pairs from  $\pi^*(q)$ . Each representative pair is checked by the G-ICP gate, and only passing pairs are inserted as loop factors. The relative pose estimated by each passing G-ICP registration is used as the loop-factor measurement. If none of the representatives pass the G-ICP gate, the query is rejected.

#### F. Practical Considerations

The online cost is dominated by evaluating a small number of descriptor segment scores and, after a query passes the calibrated boundary, the G-ICP gate. The likelihoods and acceptance boundary are calibrated offline in a leave-one-sequence-out manner. The deployment-time verifier uses descriptor scores, the learned 1D likelihoods, the scalar boundary  $a_\delta$ , and the G-ICP gate.

---

#### Algorithm 1 QCSA Loop Admission

---

**Require:** Query  $q$ , candidates  $\mathcal{T}(q)$ , hard-negative LLR map  $\ell(\cdot)$ , boundary  $a_\delta$ , G-ICP gate  $G$ .

**Ensure:** A set of loop factors or  $\emptyset$  for query  $q$ .

- 1: Form  $\mathcal{P}(q)$  from  $\mathcal{T}(q)$ , allowed directions, and horizons.
  - 2:  $\pi^*(q) \leftarrow \arg \max_{\pi \in \mathcal{P}(q)} T(\pi)$
  - 3:  $Z_q \leftarrow T(\pi^*(q))$
  - 4: **if**  $Z_q < a_\delta$  **then**
  - 5:     **return**  $\emptyset$  // abstain at evidence stage
  - 6: **end if**
  - 7: Select representative pairs  $\mathcal{R}$  from  $\pi^*(q)$ .
  - 8:  $\mathcal{F} \leftarrow \{(q_c, t_c) \in \mathcal{R} : G(q_c, t_c) \text{ passes}\}$
  - 9: **if**  $\mathcal{F} = \emptyset$  **then**
  - 10:     **return**  $\emptyset$
  - 11: **end if**
  - 12: **return** loop factors for  $\mathcal{F}$  with G-ICP relative-pose measurements
- 

## IV. DATASET AND EVALUATION

### A. SNU Library Dataset (SNULib)

SNULib targets LiDAR loop closure in long, near-identical indoor shelf-and-corridor layouts where global descriptors frequently face perceptual ambiguity. Data were recorded over five sequences with a Clearpath Jackal equipped with an Ouster OS1-128 LiDAR, IMU, and stereo camera. We obtain reference trajectories by using A-LOAM as a representative implementation of the LOAM pipeline [33], followed by hierarchical LiDAR bundle adjustment (HBA) refinement [34].

### B. Evaluation Protocol

We hold retrieval fixed and vary only the loop admission policy. All methods share loop-pair labels, candidate generation, the G-ICP gate, and the pose-graph optimization back-end. HBA-refined reference trajectories are used for calibration and evaluation, while test-time admission uses only descriptor scores and the G-ICP gate. For SNULib, all likelihoods and query-level boundaries for the proposed layer are leave-one-sequence-out (LOSO) calibrated, excluding the test sequence from each fold.

1) *Reference labels:* Reference loops are keyframe pairs whose horizontal separation is below 0.5 m and relative rotation is within  $12^\circ$  in  $SO(3)$ , with a 30 s minimum temporal separation and a 3.0 m path-length gap. For evaluation, keyframes are grouped into 0.25 m motion clusters to avoid double-counting repeated detections of the same local cell pair, and connected runs of reference-positive cluster pairs define reference segments. Likelihood fitting uses the LOSO calibration top- $M$  retrieval stream before G-ICP: scores whose motion-cluster pair is reference-positive fit  $\hat{f}_+$ , while non-adjacent ( $|c_q - c_t| > 1$ ) reference-negative scores fit  $\hat{f}_{\text{HN}}$ , using one-dimensional Gaussian KDE. For query-level calibration, we use only clear non-loop candidate segments as hard negatives. A candidate segment has reference overlap

TABLE I: SNULib loop-factor admission and downstream PGO outcome under the main operating point. The proposed policy admits at most one segment per query and inserts G-ICP-passing representative pairs. In the aggregate row, relative to Top1+G-ICP, QCSA reduces factors from 1853 to 492, raises  $P$  from 0.542 to 0.717, lowers FA/1k from 97.7 to 16.0, lowers G-ICP/q from 1.000 to 0.476, and changes 0.229/1.064 to 0.224/0.778 m ATE mean/worst.

Descriptor	QCSA						Top1+G-ICP				
	Edges	P	R	FA/1k	G-ICP/q	ATE $_{\mu/\max}$	Edges	P	R	FA/1k	ATE $_{\mu/\max}$
LiDAR Iris	64	0.688	0.093	16.1	0.506	0.229/0.695	304	0.576	0.368	103.9	0.176/0.512
ScanContext++	58	0.793	0.097	9.7	0.446	0.230/0.769	237	0.603	0.301	75.7	0.226/0.725
NDT-MC	72	0.764	0.116	13.7	0.488	0.225/0.692	260	0.546	0.299	95.1	0.251/0.821
OT	61	0.754	0.097	12.1	0.450	0.239/0.778	231	0.442	0.215	103.9	0.302/1.064
LoGG3D-Net	81	0.568	0.097	28.2	0.459	0.171/0.470	228	0.487	0.234	94.3	0.221/0.692
RING++	80	0.700	0.118	19.3	0.503	0.242/0.746	330	0.552	0.383	119.3	0.260/0.913
MinkLoc3Dv2	76	0.789	0.126	12.9	0.479	0.231/0.758	263	0.567	0.314	91.9	0.169/0.459
<b>Aggregate</b>	<b>492</b>	<b>0.717</b>	<b>0.106</b>	<b>16.0</b>	<b>0.476</b>	<b>0.224/0.778</b>	<b>1853</b>	<b>0.542</b>	<b>0.302</b>	<b>97.7</b>	<b>0.229/1.064</b>
Reference: Odometry only (no loop closure) ATE $_{\mu/\max}$ = 0.582 / 2.175 m.											

when it matches a reference segment for at least five cluster pairs, allowing gaps of up to two clusters. Candidate segments with 1–4 matched pairs are treated as ambiguous and excluded; segments with no matched pairs are eligible hard negatives.

2) *Descriptors and baselines*: We evaluate seven descriptor families: LiDAR Iris [4], ScanContext++ [3], NDT-Map-Code (NDT-MC) [6], OverlapTransformer [25], LoGG3D-Net [22], RING++ [17], and MinkLoc3Dv2 [23]. For learned descriptors, we use the publicly released pretrained checkpoints from the cited implementations without dataset- or route-specific fine-tuning; QCSA only consumes their scalar retrieval scores. The main SNULib baseline follows the common retrieve-then-verify pattern: for each query, the top-ranked retrieved database candidate under the same descriptor family is checked by the same G-ICP gate used by the proposed method and then inserted as a loop factor if it passes. We denote this baseline as Top1+G-ICP. We additionally compare against sparse Top1+G-ICP selections and SeqSLAM [27] at the same factor budget. For HeLiPR [15], we report a compact fixed-transfer overlap-admission comparison against raw Top1 retrieval, accepted-count-matched Top1, Vanilla LLR Test, and HardNeg LLR Test. Vanilla LLR Test fits the null model from generic non-loop scores, while HardNeg LLR Test fits it from hard-negative scores; both use the same fixed cumulative-LLR decision rule.

3) *Metrics*: The primary metrics are loop-factor precision  $P$ , recall  $R$ , false admissions per 1000 query groups (FA/1k), hard-negative acceptance rate (HN-acc), and G-ICP gate evaluations per query group (G-ICP/q). Here, one query group means one anchor keyframe evaluated on one sequence with one descriptor family. Pair precision  $P$  evaluates the admitted loop factors inserted into the graph: each inserted frame-pair factor is mapped to a 0.25 m motion-cluster pair, counted as TP if it is reference-positive and FP otherwise, while recall  $R$  is TP divided by the number of reference-positive cluster pairs after the same clustering. FA/1k counts false admissions per 1000 query groups, and G-ICP/q counts G-ICP gate evaluations per query group; for HeLiPR, HN-acc is the fraction of retrieved hard-negative candidates that are accepted. For downstream validation on SNULib, we run

PGO using the accepted loop factors and report mean and worst-sequence ATE RMSE.

4) *Implementation details*: Unless stated otherwise, the proposed layer uses top- $M$  candidates with  $M = 4$  after excluding the previous 25 frames, horizons  $h \in [5, 11]$ , directions  $s \in \{+1, -1\}$ , and LLR clipping to  $[-4, 4]$ . After acceptance, additional factors for the same motion-cluster pair are suppressed for 120 frames to avoid repeatedly inserting the same local loop. The main SNULib operating point uses  $\delta = 0.3$ , representative-pair insertion using first/middle/last pairs, and the precision G-ICP gate (registration fitness  $\geq 0.7$ , inlier RMSE  $\leq 0.15$  m). The same-budget sparse PGO comparison uses this operating point and truncates competing baselines to the same number of inserted factors. Given the same-floor ground-vehicle setting of SNULib, PGO is run in SE(2) with odometry noise (0.05 m,  $2^\circ$ ), loop-factor noise (0.10 m,  $5^\circ$ ), and at most 30 nonlinear function evaluations. For HeLiPR, dense trajectories are sampled at 1.0 m and query/database anchors at 10.0/5.0 m. A retrieved anchor pair is positive if the anchor distance is below 7.5 m and is counted as a hard negative for HN-acc if the distance exceeds 20.0 m; all verifier thresholds are transferred from SNULib without route-specific tuning.

## V. EXPERIMENTS

### A. Sparse Loop Admission on SNULib

Table I compares the proposed policy against Top1+G-ICP across all seven descriptors. The main setting admits at most one calibrated segment per query and checks its first, middle, and last representative pairs with G-ICP. Across all descriptor families, the policy inserts 492 loop factors versus 1853 for Top1+G-ICP, a  $3.8\times$  reduction in graph density. It also raises factor precision from 0.542 to 0.717, reduces FA/1k from 97.7 to 16.0, and runs G-ICP on 0.476 candidates per query instead of one candidate per query.

The ATE columns report the corresponding PGO outcome under the same SE(2) back-end. For consistency with all graph-level trajectory results, the odometry-only reference is reported under the same protocol: HBA pseudo-ground truth, all five sequences, XY ATE RMSE, and mean/worst-case aggregation over sequences. The bottom reference row

TABLE II: ICP-dependence audit on SNULib, aggregated over seven descriptors. The “off” rows disable the G-ICP fitness/RMSE admission gate while keeping the same retrieval streams; the “on” rows use the main precision gate.

Method	G-ICP gate	Adm.	TP	FP	P
Top1	off	7777	1073	6704	0.138
Top1	on	1853	1004	849	0.542
QCSA	off	984	356	628	0.362
QCSA	on	492	353	139	<b>0.717</b>

TABLE III: Operating-point sensitivity on SNULib. Rows vary one parameter at a time around the main setting; ATE is mean/worst-sequence RMSE.

Param.	Value	Edges	P	R	FA/1k	G-ICP/q	ATE <sub><math>\mu</math>/max</sub>
$\delta$	0.20	448	0.723	0.097	14.3	0.378	0.229/0.872
	0.25	485	0.720	0.105	15.7	0.429	0.227/0.872
	0.30	492	0.717	0.106	16.0	0.476	0.224/0.778
	0.35	502	0.709	0.107	16.8	0.520	0.224/0.778
	0.40	512	0.709	0.109	17.2	0.567	0.224/0.778
$h$	[5,7]	626	0.657	0.124	24.7	0.482	0.225/0.906
	[5,9]	550	0.680	0.112	20.3	0.478	0.224/0.903
	[5,11]	492	0.717	0.106	16.0	0.476	0.224/0.778

shows that odometry-only (loop closure disabled) yields mean ATE 0.582 m and worst-sequence ATE 2.175 m, dominated by drift on the longest sequence. The proposed policy improves aggregate mean/worst ATE from 0.229/1.064 m to 0.224/0.778 m while using substantially fewer factors. Descriptor-wise trajectory outcomes vary because sparse admission trades dense loop coverage for conservative factor insertion. We therefore emphasize the aggregate and worst-sequence behavior, together with the same-budget comparison, rather than claiming uniform per-descriptor ATE dominance. These aggregate results characterize the primary admission behavior: the calibrated layer lowers false-admission density and geometric verification load while preserving graph accuracy in the sparse insertion regime.

Table II separates descriptor-stage admission from geometric filtering. When the G-ICP fitness/RMSE gate is disabled while keeping the same retrieval streams and segment admission, the policy reduces false positives from 6704 to 628 and raises precision from 0.138 to 0.362. After the shared precision gate, false positives are further reduced from 849 to 139. The audit thus shows that descriptor-stage admission reduces the aliased candidate pool before geometry, and the shared G-ICP gate then filters the selected representative pairs.

Table III checks whether the representative setting is an isolated operating point. With the same bidirectional fixed unit-stride segment construction and precision G-ICP gate, increasing  $\delta$  admits more query-level evidence and increases factor density. The horizon sweep shows that shorter segments admit more factors but also raise false-admission density. We use  $\delta = 0.30$  and  $h \in [5, 11]$  as a practical default for the remaining SNULib experiments.

## B. Same-Budget Graph-Level Stability

We compare the proposed policy with alternative sparse insertion policies at the same factor count, with factor metrics and ATE summarized in Table IV. The budget is fixed before PGO by the main operating point in Table I, which inserts 492 loop factors across all seven descriptors. We then restrict each competing sparse baseline to that same budget. All sparse Top1 rows first run dense Top1+G-ICP and then keep 492 gated factors. The “score” row is a global descriptor-score top- $k$ , and “fitness” is a global registration-fitness top- $k$  with RMSE tie-break. The “run-balanced” row takes descriptor-score-ranked factors in round-robin order across sequence–descriptor runs, testing whether a more even budget distribution across runs is sufficient without QCSA’s query-level admission. For SeqSLAM, we apply local contrast enhancement to the same descriptor-distance matrices and then perform velocity-window sequence matching ( $d_s = 10$ ,  $R = 20$ ,  $v \in [0.8, 1.2]$ ), then rank the G-ICP-gated predictions by SeqSLAM score to form the matched 492 unique factors. At this matched budget, QCSA reports the lowest mean/worst ATE among the sparse-loop rows and uses 0.476 G-ICP checks per query. SeqSLAM is closer in ATE than the sparse Top1+G-ICP rows, but remains above QCSA. Among the sparse Top1+G-ICP baselines, fitness ranking gives the highest pair-level P/R and the lowest FA/1k, but its ATE remains higher than QCSA.

## C. LLR Baseline Failure Modes and Component Ablation

To isolate the contribution of each design choice in the proposed layer, we decompose the verifier into a chain of intermediate likelihood-ratio variants and re-run each on the SNULib evaluation pipeline. Table V reports the staged ablation over all seven descriptor families. Stage 1 is Vanilla LLR Test, using a fixed Wald boundary with a LOSO generic non-loop null. Stage 2 changes only the null model to the LOSO hard-negative null. Stage 3 keeps the hard-negative null but replaces the fixed boundary with pair-level LOSO quantile calibration. Stage 4 is the deployed query-level policy with G-ICP-validated representative-pair insertion. The fixed-boundary baselines use the strictest cumulative-LLR boundary setting from the LLR sweep (accept/reject boundaries 13.8/−6.9). The pair-quantile row uses a calibration quantile level  $\gamma = 0.99$ , while the query+segment row uses the main operating point from Table I. Replacing the LOSO generic non-loop null with the LOSO hard-negative null (Stage 2) lifts pair precision from 0.180 to 0.385 and reduces FA/1k from 559.5 to 36.8, but admitted pairs collapse because hard negatives sharpen the null and few candidates still cross the fixed boundary. Replacing the fixed boundary with per-pair LOSO quantile calibration (Stage 3) recovers many reference positives but admits 1911 pairs and raises FA/1k to 93.9, since a per-pair rule still lets multiple aliased candidates within the same query trigger. With the deployed query-level policy, Stage 4 raises pair precision to 0.717 while reducing admitted density to 0.057 Acc./q and FA/1k to 16.0. Acc./q is normalized by detector-query

TABLE IV: Same-budget sparse graph-stability comparison on SNULib. The budget is set by the main operating point in Table I; all non-odometry sparse-loop rows insert 492 loop factors over the seven descriptor families. FA/1k is false admissions per 1000 query groups.

Method	P	R	FA/1k	G-ICP/q	ATE mean	ATE max
Odometry only	–	–	–	0.000	0.582	2.175
Top1+G-ICP score	0.457	0.068	34.3	1.000	0.575	2.487
Top1+G-ICP fitness	0.770	0.114	14.5	1.000	0.605	3.018
Top1+G-ICP run-balanced	0.591	0.088	25.8	1.000	0.587	2.783
SeqSLAM	0.445	0.066	34.6	1.000	0.272	0.895
<b>QCSA</b>	0.717	0.106	16.0	<b>0.476</b>	<b>0.224</b>	<b>0.778</b>

TABLE V: Component ablation on SNULib. Each row adds one calibration or admission component to the likelihood-ratio verifier; Stage 4 is the deployed G-ICP-gated policy at the main operating point in Table I.

Stage	Variant	TP/FP	Acc.	Pair P	Acc./q	FA/1k
1	Vanilla LLR Test	1067/4860	5927	0.180	0.682	559.5
2	+ HN null	200/320	520	0.385	0.060	36.8
3	+ Pair quantile	1095/816	1911	0.573	0.220	93.9
4	+ Query+segment	353/139	492	0.717	0.057	16.0

groups; FA/1k is false admissions per 1000 detector-query groups.

Together, the internal ablation and external fixed-transfer results show how hard-negative evidence and query-level admission affect false-admission density across internal and public-route settings.

#### D. External HeLiPR Overlap Validation

We evaluate fixed-transfer admission using four HeLiPR [15] Bridge sequences and seven descriptor families with library-derived thresholds, without route-specific tuning. This experiment checks whether the library-derived hard-negative calibration suppresses far false matches on an external route family. Table VI compares the proposed policy with raw Top1 retrieval, accepted-count-matched Top1, and LLR-test verifier baselines. The Top1@same-Acc row controls for sparsity by matching the accepted count to QCSA using descriptor-distance ranking. At the same accepted count (1037), QCSA changes TP/FP from 897/140 to 929/108, raising precision from 0.865 to 0.896 and reducing FA/1k from 82.3 to 63.5. Compared with HardNeg LLR Test, QCSA reduces accepted false pairs from 491 to 108 and HN-acc from 0.046 to 0.029.

#### E. Wallclock Runtime

At the main setting ( $\delta = 0.30$ ), the proposed policy runs G-ICP on 0.476 candidate pairs per query on average across the SNULib evaluation in Table I. On SNULib sequence 3 (329 queries, single thread, AMD Ryzen 7 5800X, 64 GB RAM), the descriptor-stage overhead is 2.47–2.66 ms/query over three repeats per descriptor, excluding offline LOSO calibration (mean 2.58 ms). Descriptor extraction and score-matrix construction are shared across policies and are outside this timing; the reported overhead measures QCSA admission from descriptor scores before the separately timed G-ICP registrations. Offline calibration is performed once per

TABLE VI: Compact HeLiPR fixed-transfer overlap validation. Top1 accepts the descriptor rank-1 candidate for each query. Top1@same-Acc keeps the same per-run/descriptor accepted count as the proposed policy using descriptor-distance ranking. All metrics are aggregated over the same seven descriptor families and four Bridge-sequence evaluations. FA/1k is false admissions per 1000 query groups; HN-acc is retrieved hard-negative acceptance rate.

Policy	Acc.	TP/FP	P	R	FA/1k	HN-acc
Top1	1701	1396/305	0.821	0.388	179.3	0.104
Top1@same-Acc	1037	897/140	0.865	0.249	82.3	0.030
Vanilla LLR Test	3203	1976/1227	0.617	0.549	721.3	0.238
HardNeg LLR Test	1636	1145/491	0.700	0.318	288.7	0.046
<b>QCSA</b>	1037	929/108	<b>0.896</b>	0.258	<b>63.5</b>	<b>0.029</b>

LOS0 fold and is not on the deployment critical path. On this aliasing-heavy sequence, the policy runs G-ICP on 0.62–0.79 candidates/query (mean 0.723), while Top1+G-ICP runs geometry on every query. Timing 3241 unique sequence-3 G-ICP gate evaluations sampled from the Top1+G-ICP and QCSA runs on the same workstation gives mean/median/p95 costs of 224.2/208.6/335.7 ms. This yields expected online verifier costs of 224.2 ms/query for Top1+G-ICP and  $2.58 + 0.723 \times 224.2 = 164.6$  ms/query for the proposed policy.

## VI. CONCLUSION

This paper presented QCSA, a descriptor-agnostic sparse loop-admission layer for LiDAR SLAM in structurally repetitive environments. QCSA scores short descriptor segments against a hard-negative null, calibrates admission at the query level, and inserts G-ICP-validated representative pairs into the pose graph. The resulting policy is intended to admit a compact set of loop factors that is less likely to damage downstream pose-graph optimization under strong aliasing.

Across seven LiDAR descriptor families on SNULib, QCSA produced a much sparser factor set than dense Top1+G-ICP while increasing loop-factor precision, reducing false admissions and G-ICP calls per query group, and improving worst-sequence ATE with comparable mean ATE. The matched-budget study further showed that selecting the same number of G-ICP-passing factors by descriptor score, registration fitness, or run-balanced ranking did not provide the same downstream trajectory behavior. These results suggest evaluating sparse loop admission by both factor-level labels and graph-level trajectory outcome.

Fixed-transfer tests on four HeLiPR Bridge sequences provided an external check on public-route data without route-specific tuning. In these tests, QCSA reduced accepted hard-negative matches compared with LLR-test and count-matched Top1 baselines while using thresholds transferred from the library calibration. The main limitations are the precision-first recall trade-off and the still-limited public-data coverage. Future work will study broader outdoor route families and adaptive calibration when the retrieval distribution changes over time.

## REFERENCES

- [1] S. Thrun, W. Burgard, and D. Fox, *Probabilistic Robotics*. MIT Press, 2005.
- [2] C. Cadena, L. Carlone, H. Carrillo, Y. Latif, D. Scaramuzza, J. Neira, I. Reid, and J. J. Leonard, “Past, present, and future of simultaneous localization and mapping: Toward the robust-perception age,” *IEEE Transactions on robotics*, vol. 32, no. 6, pp. 1309–1332, 2016.
- [3] G. Kim, S. Choi, and A. Kim, “Scan context++: Structural place recognition robust to rotation and lateral variations in urban environments,” *IEEE Transactions on Robotics*, vol. 38, no. 3, pp. 1856–1874, 2022.
- [4] Y. Wang, Z. Sun, C.-Z. Xu, S. E. Sarma, J. Yang, and H. Kong, “Lidar iris for loop-closure detection,” in *2020 IEEE/RSJ International Conference on Intelligent Robots and Systems (IROS)*. IEEE, 2020, pp. 5769–5775.
- [5] Y. Fan, X. Du, L. Luo, and J. Shen, “Fresco: Frequency-domain scan context for lidar-based place recognition with translation and rotation invariance,” in *2022 17th International Conference on Control, Automation, Robotics and Vision (ICARCV)*. IEEE, 2022, pp. 576–583.
- [6] L. Liao, W. Yan, L. Sun, X. Bai, Z. You, H. Yuan, and C. Fu, “Ndt-map-code: A 3d global descriptor for real-time loop closure detection in lidar slam,” in *2024 IEEE/RSJ International Conference on Intelligent Robots and Systems (IROS)*. IEEE, 2024, pp. 7854–7861.
- [7] C. Yuan, J. Lin, Z. Liu, H. Wei, X. Hong, and F. Zhang, “Btc: A binary and triangle combined descriptor for 3-d place recognition,” *IEEE Transactions on Robotics*, vol. 40, pp. 1580–1599, 2024.
- [8] S. Gupta, T. Guadagnino, B. Mersch, I. Vizzo, and C. Stachniss, “Effectively detecting loop closures using point cloud density maps,” in *2024 IEEE International Conference on Robotics and Automation (ICRA)*. IEEE, 2024, pp. 10 260–10 266.
- [9] A. Geiger, P. Lenz, and R. Urtasun, “Are we ready for autonomous driving? the kitti vision benchmark suite,” in *2012 IEEE conference on computer vision and pattern recognition*. IEEE, 2012, pp. 3354–3361.
- [10] G. Kim, Y. S. Park, Y. Cho, J. Jeong, and A. Kim, “Mulran: Multimodal range dataset for urban place recognition,” in *2020 IEEE international conference on robotics and automation (ICRA)*. IEEE, 2020, pp. 6246–6253.
- [11] M. Ramezani, Y. Wang, M. Camurri, D. Wisth, M. Mattamala, and M. Fallon, “The newer college dataset: Handheld lidar, inertial and vision with ground truth,” in *2020 IEEE/RSJ International Conference on Intelligent Robots and Systems (IROS)*. IEEE, 2020, pp. 4353–4360.
- [12] K. L. Ho and P. Newman, “Detecting loop closure with scene sequences,” *International journal of computer vision*, vol. 74, no. 3, pp. 261–286, 2007.
- [13] Y. Latif, C. Cadena, and J. Neira, “Robust loop closing over time,” in *Proc. Robotics: Science Systems*, 2013, pp. 233–240.
- [14] N. Sünderhauf and P. Protzel, “Switchable constraints for robust pose graph slam,” in *2012 IEEE/RSJ International Conference on Intelligent Robots and Systems*. IEEE, 2012, pp. 1879–1884.
- [15] M. Jung, W. Yang, D. Lee, H. Gil, G. Kim, and A. Kim, “Helipr: Heterogeneous lidar dataset for inter-lidar place recognition under spatiotemporal variations,” *The International Journal of Robotics Research*, vol. 43, no. 12, pp. 1867–1883, 2024.
- [16] G. Kim and A. Kim, “Scan context: Egocentric spatial descriptor for place recognition within 3d point cloud map,” in *2018 IEEE/RSJ International Conference on Intelligent Robots and Systems (IROS)*. IEEE, 2018, pp. 4802–4809.
- [17] X. Xu, S. Lu, J. Wu, H. Lu, Q. Zhu, Y. Liao, R. Xiong, and Y. Wang, “Ring++: Roto-translation invariant gram for global localization on a sparse scan map,” *IEEE Transactions on Robotics*, vol. 39, no. 6, pp. 4616–4635, 2023.
- [18] L. He, X. Wang, and H. Zhang, “M2dp: A novel 3d point cloud descriptor and its application in loop closure detection,” in *2016 IEEE/RSJ International Conference on Intelligent Robots and Systems (IROS)*. IEEE, 2016, pp. 231–237.
- [19] R. Dubé, D. Dugas, E. Stumm, J. Nieto, R. Siegwart, and C. Cadena, “Segmatch: Segment based place recognition in 3d point clouds,” in *2017 IEEE international conference on robotics and automation (ICRA)*. IEEE, 2017, pp. 5266–5272.
- [20] M. A. Uy and G. H. Lee, “Pointnetvlad: Deep point cloud based retrieval for large-scale place recognition,” in *Proceedings of the IEEE conference on computer vision and pattern recognition*, 2018, pp. 4470–4479.
- [21] Z. Liu, S. Zhou, C. Suo, P. Yin, W. Chen, H. Wang, H. Li, and Y.-H. Liu, “Lpd-net: 3d point cloud learning for large-scale place recognition and environment analysis,” in *Proceedings of the IEEE/CVF international conference on computer vision*, 2019, pp. 2831–2840.
- [22] K. Vidanapathirana, M. Ramezani, P. Moghadam, S. Sridharan, and C. Fookes, “Logg3d-net: Locally guided global descriptor learning for 3d place recognition,” in *2022 International Conference on Robotics and Automation (ICRA)*. IEEE, 2022, pp. 2215–2221.
- [23] J. Komorowski, “Improving point cloud based place recognition with ranking-based loss and large batch training,” in *2022 26th international conference on pattern recognition (ICPR)*. IEEE, 2022, pp. 3699–3705.
- [24] X. Chen, T. Läbe, A. Milioto, T. Röhring, J. Behley, and C. Stachniss, “Overlapnet: A siamese network for computing lidar scan similarity with applications to loop closing and localization,” *Autonomous Robots*, vol. 46, no. 1, pp. 61–81, 2022.
- [25] J. Ma, J. Zhang, J. Xu, R. Ai, W. Gu, and X. Chen, “Overlaptransformer: An efficient and yaw-angle-invariant transformer network for lidar-based place recognition,” *IEEE Robotics and Automation Letters*, vol. 7, no. 3, pp. 6958–6965, 2022.
- [26] J. Ma, X. Chen, J. Xu, and G. Xiong, “Seqot: A spatial-temporal transformer network for place recognition using sequential lidar data,” *IEEE Transactions on Industrial Electronics*, vol. 70, no. 8, pp. 8225–8234, 2022.
- [27] M. J. Milford and G. F. Wyeth, “Seqslam: Visual route-based navigation for sunny summer days and stormy winter nights,” in *2012 IEEE international conference on robotics and automation*. IEEE, 2012, pp. 1643–1649.
- [28] M. Cummins and P. Newman, “Fab-map: Probabilistic localization and mapping in the space of appearance,” *The International journal of robotics research*, vol. 27, no. 6, pp. 647–665, 2008.
- [29] P. Agarwal, G. D. Tipaldi, L. Spinello, C. Stachniss, and W. Burgard, “Robust map optimization using dynamic covariance scaling,” in *2013 IEEE international conference on robotics and automation*. IEEE, 2013, pp. 62–69.
- [30] E. Olson and P. Agarwal, “Inference on networks of mixtures for robust robot mapping,” *The International Journal of Robotics Research*, vol. 32, no. 7, pp. 826–840, 2013.
- [31] N. Sünderhauf and P. Protzel, “Switchable constraints vs. max-mixture models vs. rrr-a comparison of three approaches to robust pose graph slam,” in *2013 IEEE International Conference on Robotics and Automation*. IEEE, 2013, pp. 5198–5203.
- [32] A. N. Angelopoulos and S. Bates, “Conformal prediction: A gentle introduction,” *Foundations and Trends in Machine Learning*, vol. 16, no. 4, pp. 494–591, 2023.
- [33] J. Zhang, S. Singh *et al.*, “Loam: Lidar odometry and mapping in real-time,” in *Robotics: Science and systems*, vol. 2, no. 9. Berkeley, CA, 2014, pp. 1–9.
- [34] X. Liu, Z. Liu, F. Kong, and F. Zhang, “Large-scale lidar consistent mapping using hierarchical lidar bundle adjustment,” *IEEE Robotics and Automation Letters*, vol. 8, no. 3, pp. 1523–1530, 2023.